

Eliminating the limiting-current phenomenon by geometric field focusing into nanopores and nanoslots

Gilad Yossifon,* Peter Mushenheim, Yu-Chen Chang, and Hsueh-Chia Chang[†]

Department of Chemical and Biomolecular Engineering, Center for Microfluidics and Medical Diagnostics, University of Notre Dame, Notre Dame, Indiana 46556, USA

(Received 3 October 2009; published 5 April 2010)

A peculiar and undesirable current-voltage characteristic of nanoporous membranes is that it exhibits a voltage window with a near-constant limiting-current density when bulk ions near one surface of the membrane are depleted. We show both theoretically and experimentally that this interval disappears for an isolated circular nanopore (or narrow nanoslot) because radial field focusing at the pore entrance enhances the depletion effect and drives an ejecting hydrodynamic vortex pair that amplifies ion flux into the nanopore. This vortex pair is distinct from the vortex arrays that appear in front of a wide nanoslot or a nanoporous membrane with small inter-nanopore separation. It hence suggests that an optimal pore radius/separation ratio exists for maximum current density across a membrane.

DOI: 10.1103/PhysRevE.81.046301

PACS number(s): 47.61.Fg, 47.57.jd, 82.39.Wj, 47.20.Ma

I. INTRODUCTION

A curious and important *I-V* characteristic of conducting ion-selective (nanoporous) membranes, such as those in fuel cells, solar cells, mammalian cells with ion channels and desalination devices, is that, at sufficiently high voltages, the current *I* deviates from the usual linear Ohmic dependence on the voltage *V*. More specifically [see Fig. 1(a)], at some voltage threshold, the differential resistance increases to a large but finite value. Beyond yet another critical “gating” voltage, the differential resistance decreases again to a level that is comparable with that in the Ohmic region. The former part of the *I-V* curve is referred to as the “limiting-resistance” region, while the latter is referred to as the “over-limiting” current region (e.g., [1]). (The middle high-resistance region is often referred to as the limiting-current region [2] but it is more aptly described as a limiting-resistance region with high but finite limiting differential resistance, as the current does not necessarily approach a limiting value.) The high resistance in this region limits the current density of fuel/solar cells and is an important factor in the overall efficiency of these devices.

A straight nanochannel or more accurately nanoslot (since the standard photolithography techniques cannot produce a width that approaches the submicron length scale of its height) is a simple model (Fig. 2) for an ion-selective nanoporous membrane, as the electric Debye layers (EDLs) of both top and bottom substrates overlap as in a nanopore. Like an ion-selective membrane, the overlapping double layers select the counterions to carry most of the current across the slot. In recent years, fabrication of nanochannels has become possible and the ion transport (e.g., [3]), ion-enrichment, and ion-depletion (e.g., [4,5]), rectification of ionic current (e.g., [6]), limiting and overlimiting-current [7]

phenomena have been examined with these pseudo-ion selective membranes.

While these nonlinear *I-V* features were previously studied for pseudohomogenous nanoporous membranes with high pore connectivity [8] and recently for wide nanoslots [9], the case of a single nanopore (or equivalently, a narrow nanoslot) with three-dimensional field-focusing effects is yet

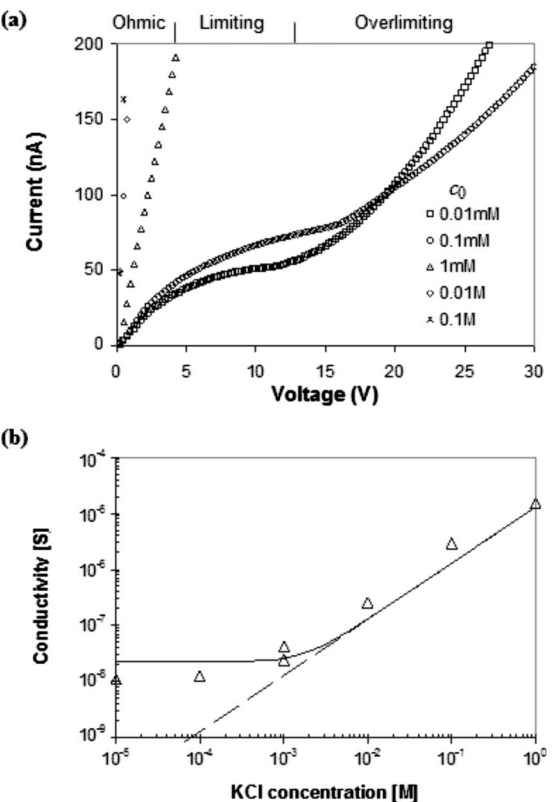


FIG. 1. (a) *I-V* characteristics of the widest nanoslot (2.5 mm) for varying ionic strengths (c_0); (b) Conductance of aqueous-filled, Polysilicon/Pyrex glass, nanoslot as a function of c_0 . [symbols—experiment; continuous line—model (18); dashed line—bulk conductivity (model (18) with $\bar{\Sigma}=0$)].

*Present address: Faculty of Mechanical Engineering, Micro- and Nanofluidics Laboratory, Technion—Israel Institute of Technology, Technion City 32000, Israel.

[†]Corresponding author: hchang@nd.edu

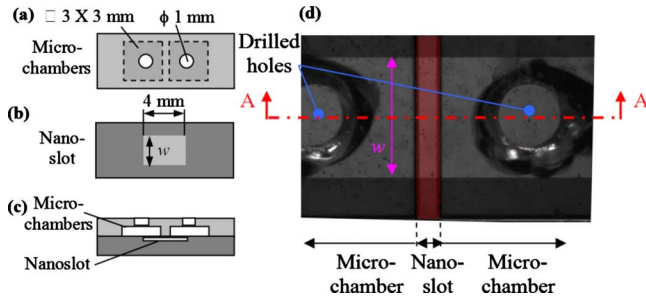


FIG. 2. (Color online) Schematic of the two Pyrex slides (top view) consisting the chip: (a) Two square microchambers of $50\ \mu\text{m}$ depth that were wet-etched into a 1 mm Pyrex glass slide. Inlet/outlet access holes were mechanically drilled into the center of each microchamber; (b) Rectangle of varying width w ($=2.5, 1, 0.5\ \text{mm}$, and $50\ \mu\text{m}$) and depth $H=190\ \text{nm}$, that is etched into the deposited polysilicon layer on top of a second 1 mm Pyrex glass slide; (c) Sealing of these two glass slides form the nanoslot that connects the two microchambers as seen in the side-view that corresponds to the cross-section A-A of the chip; (d) Optical microscope image (top view) of the chip with the widest (2.5 mm) nanoslot (emphasized with red background).

to be scrutinized. Transport issues important at the single nanopore level are mostly neglected (or averaged out) when describing bulk membranes consisting of many nanopores [8]. However, they are expected to become important when the pore separation is sufficiently large such that the interaction among pores does not smooth out the point-sink nature of each pore with respect to field and current flux. As the electromigration ion flux in the electroneutral bulk is controlled by the gradient of the electric potential, which satisfies the Laplace equation in this space charge-free region, the flux density is expected to reflect the equation's classical fundamental solutions with constant, $1/r$ and $1/r^2$ field strengths (r being the radial coordinate) for planar, line, and point sinks. Since these fundamental solutions exhibit extremely different field strengths and length scales (see Sec. IV), it is quite possible that the different geometries can produce fundamentally different I - V characteristics. Phenomena involving space charge generation and electrohydrodynamics will be shown to appear with enhanced field focusing to increase the ion flux. Hence, nanoporous membranes with large pore separation and surface heterogeneities may produce a larger overall current even if their void fraction is smaller.

There is another development in nanotechnology that requires the understanding of current flux through isolated nanopores/slots. In recent years, artificially engineered membrane [10] or artificially fabricated [11] nanopores have been shown to be able to capture single-molecule passage events. The fabricated nanopores are often isolated to prevent cross-talk. Also, higher current density translates into higher electro-osmotic convection or higher electromigration flux of the molecular targets. Thus, understanding the electrokinetics of isolated nanochannels can help design future sensitive single-pore biosensors that can detect a specific molecule (e.g., by using surface molecular probes).

In this study, a nanoslot with varying widths is fabricated on a chip (Fig. 2) as a simple model to capture the geometric

field-focusing transition from a line (wide nanoslot) to a point (narrow nanoslot) sink. The advantages of using the two-dimensional nanoslot chip, fabricated using standard photolithography techniques, to image the concentration-polarization phenomenon were already demonstrated in [9,12]—the concentration fields and dynamics are much more amenable to confocal characterization than three-dimensional nanopore structures. Also, the photolithography technique allows precise control of the nanoslot geometry to produce gradual enhancement of the field-focusing effect (by decreasing the nanoslot width) and to eliminate the need for more sophisticated nanofabrication tools, e.g., focused-ion-beam (FIB) and electron-beam (E-Beam).

The threshold current at which the limiting-resistance region occurs is often approximated by the classical diffusion-limited current transport theory [2], according to which the current density saturates at a constant limiting-current density with an infinite differential resistance. An electroneutral diffusion layer (DL) with an ion concentration gradient appears near one of the two membrane interfaces to enhance the flux via diffusion. (This interface is on the side where the counterions enter the membrane, the side that controls the ion flux into the membrane.) This diffusive-flux enhanced current density saturates when the ion concentrations vanish at that interface to produce the limiting current—the electrolyte is effectively deionized at that location [2].

Latter theories by Rubinstein and Shtilman [8] suggest that, at higher voltages, an extended polarized layer with space charge (EPL, or equivalently, space charge layer—SCL) much thicker than the EDL can appear between the EDL and the electroneutral diffusion layer to sustain an overlimiting-current density, which is much higher than the limiting-current density [Fig. 1(a)]. The collection of these three different layers is termed the concentration-polarization layer (CPL). Starting with Rubinstein and Shtilman [8], latter studies have offered one-dimensional (1D) models of either an ideal [13] or nonideal [14] permselective nanoporous membrane. Such one-dimensional models treat the nanoporous membrane as a continuum and neglects field-focusing effects through the nanopores. The small cross-section area of the pore, compared to the cross-section area of the same flux tube outside the pore, enhances intrapore resistance to ion current. As a result, models and theories which omit this field effect often mistakenly attribute the dominant resistance below the limiting current to be in the DL outside the membrane instead of intrapore resistance due to field focusing.

Recently, we have explained and quantitatively captured [9] the nonlinear features of the entire I - V curve of a nanoslot based on a pseudo-one-dimensional model that includes field-focusing effect and the CPL, whose length was measured directly from experiments. The nanoslot entrance was assumed to be wide enough such that lateral variations can be neglected, thus resulting in a pseudo-two-dimensional geometry in cross-section. Furthermore, by realizing that the ratio between the microchamber height and that of the nanoslot is very high ($\sim 10^4$), the two-dimensional geometry was effectively collapsed onto a pseudo-one-dimensional geometry with a radial coordinate in the microchambers and a longitudinal Cartesian coordinate in the nanoslot.

A key parameter in the one-dimensional model is the thickness of the CPL near the membrane. Rubinstein *et al.*

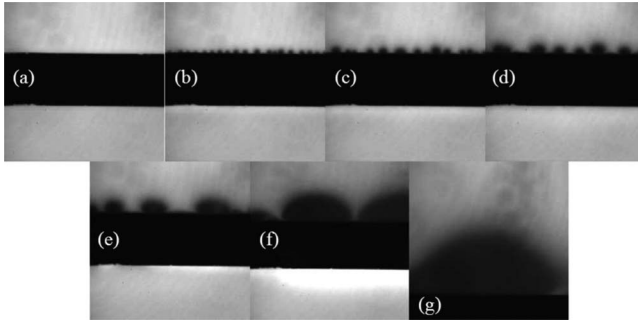


FIG. 3. Sequence showing the depletion layer pattern evolution as a response to a stepwise application of 30 V across the wide (2.5 mm) nanoslot. In particular, the complex process of wavelength selection by small vortices break up through fusion and transformation into still larger vortices until a quasisteady like pattern is formed is clearly seen.

[15] suggested a possible physical mechanism for selecting the CPL dimension that involves an intrinsic instability of the SCL (see also [16] and references therein). The lateral osmotic pressure gradient of this vortex instability produces a vortex array (Fig. 3) that specifies the thickness of the CPL which, in turn, controls the overlimiting-current density. This mechanism, although consistent with some indirect experimental observations ([1,17]), was only recently verified experimentally both with a nanoslot model [12] and a real membrane [18]. A predictive theory for this selected CPL thickness has not yet appeared and we have used the measured value in our model to quantitatively capture the entire *I-V* curve of a wide nanoslot [9]. If the CPL length scale for a real membrane can be measured empirically or derived theoretically, the model can also be extended to capture its *I-V* characteristics.

This CPL-selecting instability manifests itself in an array of vortices with a periodic depletion layer pattern of a characteristic wavelength [12]. In the case of a sufficiently wide nanoslot, the corners/side walls constitute only a small portion of the entire entrance width, and hence the singular electric fields that may be present there can be neglected at small enough voltages. Such corner effects are expected to become important for narrower slots and have been shown to produce corner vortices by the induced-charge electro-osmosis (ICEO) phenomenon [20,21]. Here we will show that there is another mechanism for the occurrence of corner vortices resulting from the combined field focusing (i.e., strong tangential electric fields) and space charge effects, known as electroosmosis of the second kind [22]. These vortices are different from the vortex array driven by Rubinstein's instability under pseudohomogenous membrane conditions. They can even suppress the instability and significantly alter the onset voltages of the limiting-resistance and overlimiting regions. As corner vortices are not observed for communicating nanopores [18], it is expected that pore isolation is necessary for their appearance. As such, the *I-V* characteristics of isolated pores can be dramatically different from communicating ones. This pore communication effect is most likely related to another well-known empirical fact. It is known that nonuniformity on the membrane can reduce the

voltage range of the undesirable limiting-resistance window. A theory concerning electroconvection predicts a reduction in the window for membranes with increased conductive or geometrical heterogeneity [15]. This was also recently experimentally verified [23], wherein reduction in up to 60% in the voltage window of the undulated membranes was obtained compared to that of a flat membrane. The heterogeneity presumably increases the isolation of the pores and also produces localized and isolated space charge regions that can sustain the corner vortex pairs.

Here, we extend previous studies on the nonlinear *I-V* characteristics of pseudo-one-dimensional membranes [8,13] and two-dimensional wide nanoslots [9] to isolated nanochannels (i.e., narrow nanoslots) and relate them to the three-dimensional field-focusing effects of isolated axisymmetric nanopores. We demonstrate the existence of the corner vortices for narrow nanoslots and show how these are related to the occurrence of a toroidal vortex in front of a nanopore. Moreover, we show how the nonlinear *I-V* features of a narrow nanoslot can be captured with an axisymmetric nanopore model when the former width becomes comparable to that of the depletion layer size. Furthermore, we demonstrate, for the first time for nanochannels, how the limiting-resistance window decreases with decreasing nanoslot entrance width and attribute it directly to the gradual change in field-focusing effects from a line source to a point source and the appearance of an ejecting vortex pair at the corners. This corner vortex pair has replaced the vortex array due to Rubinstein's instability to dictate the *I-V* characteristics. The same phenomenon is expected for real membranes with separated pores.

II. EXPERIMENTAL TECHNIQUES AND METHODS

Nanofluidic slots of different widths were fabricated to connect between two microchambers. The fabrication technique is similar to the anodic bonding procedure of Kutchoukov *et al.* [24]. Briefly, nanoslots 0.5 mm long but of different widths 2.5, 1, 0.5 mm, and 50 μm were patterned on a 190 nm thick polysilicon layer deposited on a 1 mm thick Pyrex glass (Corning 7740) substrate (Fig. 2) using standard photolithography techniques. A reactive CF_4/O_2 plasma then etched into the polysilicon layer at a rate of 100 nm/min. The depth of the resulting channel was determined by the thickness of the polysilicon layer (i.e., $H=190$ nm) as was verified using an α -stepper profilometer. The microchambers $3 \times 3 \text{ mm}^2$ were patterned on a second 1 mm thick Pyrex glass slide on which masking layers of Cr/Au (30/300 nm) were deposited. After developing through the mask layers, the microchambers were wet-etched using 52% HF solution for a predetermined time to achieve a depth of about 50 μm . Two entrance holes 1 mm in diameter were then drilled in the center of each microchamber and the rest of the masking layers were etched away using a Cr- and Au-etchants [Fig. 2(a)]. After cleaning in HNO_3 solution for about 10 min, the two slides were bonded together [Figs. 2(c) and 2(d)]. To ensure good bonding, the wafers were preheated for 2 h at 400 °C and bonded at the same temperature at 1000 V for 1 h. Reservoirs made of flexible silicon (FastwellTM

from Grace bio-Laboratories) were used on top of the openings wherein platinum electrodes were introduced. The nanoslot was filled by introducing distilled, deionized ($18 \text{ M}\Omega \text{ cm}$) water into the large fluidic reservoirs and allowing capillary forces to draw the water across the nanoslot. The electrical voltage source and I - V converter (Agilent Technologies, 4155 B Semiconductor Parameter Analyzer) were connected to the fluidic channel with negligible resistive loss via Platinum wires inserted into the reservoirs. The channels were cleaned of ionic contaminants using electrophoretic pumping. The ionic current was observed to decay while 10 V were applied across the channels to drive out ionic impurities. The reservoirs were periodically flushed with fresh solution until the current equilibrated to a minimum, which typically took ~ 20 min. This procedure was also followed by displacing different dilutions of a 1 M potassium chloride (KCl) solution to change the ionic strength and control the degree of EDL overlap.

To obtain the measured I - V curves in Figs. 1 and 4, the applied voltage was stepped in 0.25 V increments every 3 s, during which time current transients were observed to decay completely. In the low concentration limit, the three distinct I - V regimes for the wide nanoslot are indeed observed: a linear Ohmic region, followed by a limiting-resistance region with a small slope (large limiting differential resistance) and finally an overlimiting region [Fig. 1(a)]. These data are in qualitative agreement with previous experimentally obtained I - V curves for true nanoporous membranes ([1], [17]) and also for nanochannels [7,9]. It is quite clear that a limiting-resistance region is not discernable for the narrow slots (Fig. 4) and there seems to be a direct transition from the Ohmic to the overlimiting region. In the following, we suggest that this disappearance of the limiting-resistance region is due to the severe ionic concentration gradients (resulting, effectively, in a much shorter depletion region or CPL) and the ejecting vortex pair sustained by enhanced field focusing at the pointlike narrow nanoslot.

At high enough concentrations ($>10^{-3} \text{ M}$), only the Ohmic region is observed [Fig. 1(a)], irrespective of the nanoslot width. The thinner Debye length stipulates that EDLs do not overlap within the slot and the nanochannel's perm-selectivity, space charge, and superior conductivity are lost—it is no longer a model for an ion-selective nanoporous membrane. Note that the conductance at the low-voltage

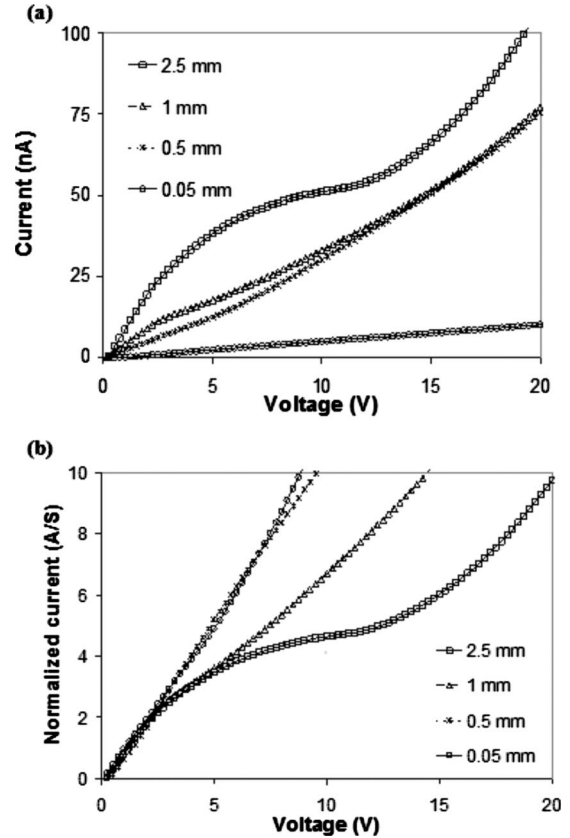


FIG. 4. (a) I - V characteristics of nanoslots with varying widths at 10^{-5} M KCl concentration; (b) the same data but normalized by the corresponding conductivity value (Ohmic region), so as to emphasize the differences in the limiting-resistance region.

Ohmic region does not scale linearly with the ionic strength at its low values [Fig. 1(b)], suggesting that intraslot resistance is important. Ohmic resistance is hence not just due to external resistance, as is assumed in earlier theories involving an infinitely conducting membrane [2]. The conductivity within the slot is finite and must be considered to quantitatively capture the true I - V characteristics [9].

In order to visualize the polarized regions, we used positive-charged Rhodamine dye molecules (counterions of the nanoslot) at $10 \mu\text{M}$ concentration. When a large enough electric field, beyond the critical voltage for the limiting-

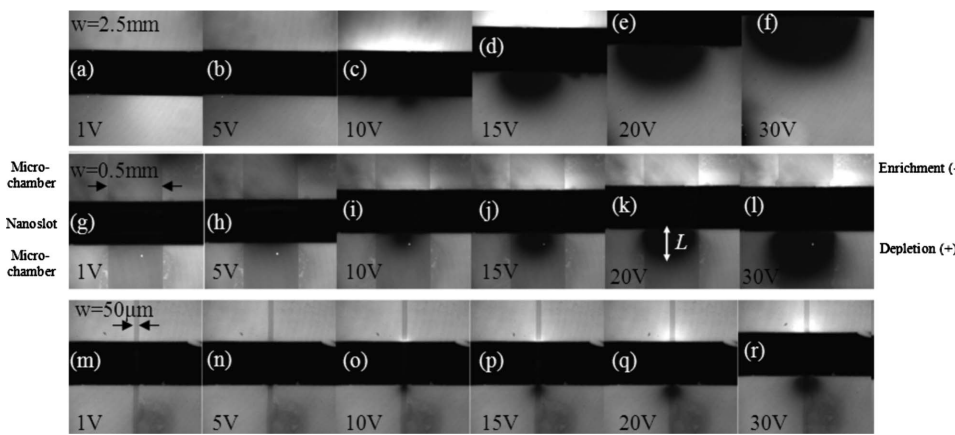


FIG. 5. Confocal image snapshots of the quasisteady depletion-enrichment layers occurring at the nanoslot opposite entrances for 10^{-5} M KCl concentration buffer at different voltage levels and nanoslot width: 2.5 mm (a)–(f), 0.5 mm (g)–(l), $50 \mu\text{m}$ (m)–(r).

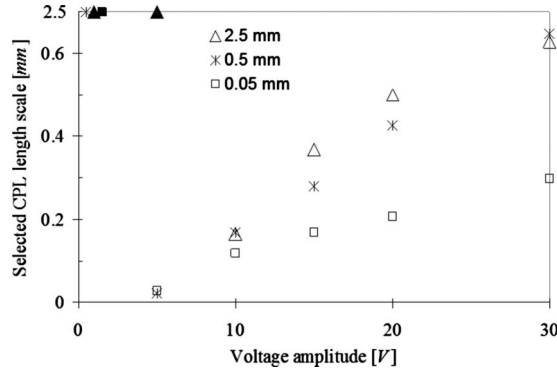


FIG. 6. The instability selected CPL length scale (L —as measured from Fig. 5) versus the applied voltage for varying nanoslots width. Filled symbols stand for cases when there is no observable vortex array (depletion array). It is then assumed that the depletion layer extends all the way to the electrodes.

resistance region, is applied across the nanoslot, an enrichment region at the cathodic entrance of the nanoslot is observed with high dye concentration while a depletion region is observed at the anodic side where the dye enters the nanoslot, as seen in Fig. 5 for the nanoslots of different width. Instead of a periodic array of depletion regions observed on the anodic side of the wide nanoslot (Fig. 3), a single and significantly smaller depletion region is obtained for the narrow nanoslot [Figs. 5(n)–5(r)]. This is also confirmed by plotting the selected depletion layer length (defined as L in Fig. 5), which approximates the selected CPL length scale [12], for nanoslots of different widths at different applied voltages (Fig. 6). At voltages below ~ 5 V for narrow and ~ 10 V for wide nanoslots (Fig. 6), it was hard to discern any depletion and the CPL length scales (see also Fig. 5). It was hence assumed that the CPL extends all the way to the electrodes (~ 2.5 mm), as indicated by the filled symbols in Fig. 6. The critical voltage in Fig. 6, when the observed CPL length undergoes a discontinuous drop, is in agreement with the onset voltage of the overlimiting region in Fig. 4. Beyond this critical voltage, the depletion is clearly discernible at the anodic side of the nanoslot interface and became more pronounced with voltage. The CPL length increased with voltage until it reached again the slot-electrode separation. However, compared to conditions below the overlimiting region, the concentration gradient in the CPL is much higher and increases with decreasing slot width. That the ionic concentration gradients in the depletion layer of the narrower nanoslot are more severe is clearly seen in Fig. 7(c), which compares the concentration profiles of different slots at 10 V. Figures 7(a) and 7(b) depict the voltage dependence of the concentration profile on the applied voltage for the wide (2.5 mm) and narrow ($50 \mu\text{m}$) nanoslots, respectively. It clearly shows the increase of the total CPL length scale in Fig. 6 and also the emergence of the polarized layer (SCL), with a flattened concentration profile inside the high-gradient depletion region, at higher voltages. These concentration plots were extracted from the fluorescent intensity profile across the depletion region at the anodic side of the nanoslot.

In order to visualize, in a qualitative manner, the inner flow structure of these depletion regions, we used fluorescent

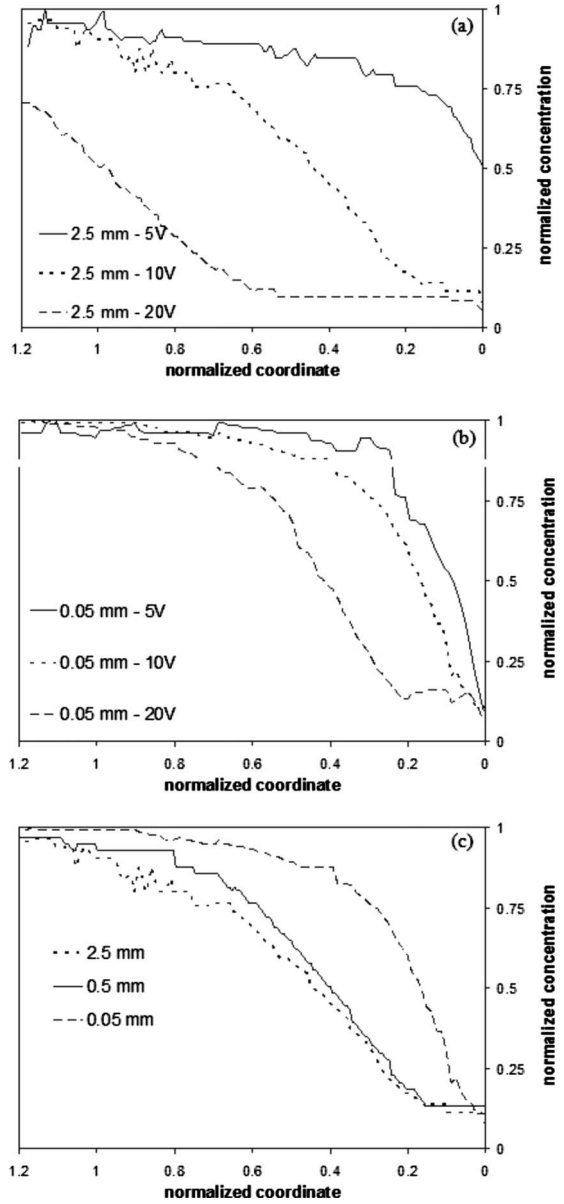


FIG. 7. Normalized concentration profile of the depletion layer at the anodic side of the (a) wide (2.5 mm) and (b) narrow ($50 \mu\text{m}$) nanoslots for different applied voltages. The normalized (by the nanoslot length) profile coordinate origin is at the nanoslot entrance at the anodic side and points into the microchamber. Part (c) of the figure compares the different concentrations profile at 10 V applied voltage for the different nanoslot widths, clearly showing increase in concentration gradient with decreasing nanoslot widths.

polymer microbeads (Duke Technologies) of $1.2 \mu\text{m}$ in size and 0.02% volumetric concentration, reminiscent of the microparticle imaging velocimetry ($\mu\text{-PIV}$) technique used for quantitative determination of the velocity field (e.g., [20]). In the case of a wide nanoslot (Figs. 8(a)–8(d)), an array of depletion regions appear, with each region encompassing a single vortex pair [12] (see the schematic vortex streamlines in Fig. 8(c), and the supplementary video [19]). Individual vortex pairs in the array appear at different locations along the nanoslot entrance. The bright spots in Figs. 8(b)–8(d) are the stagnation points of the different vortex pairs where col-

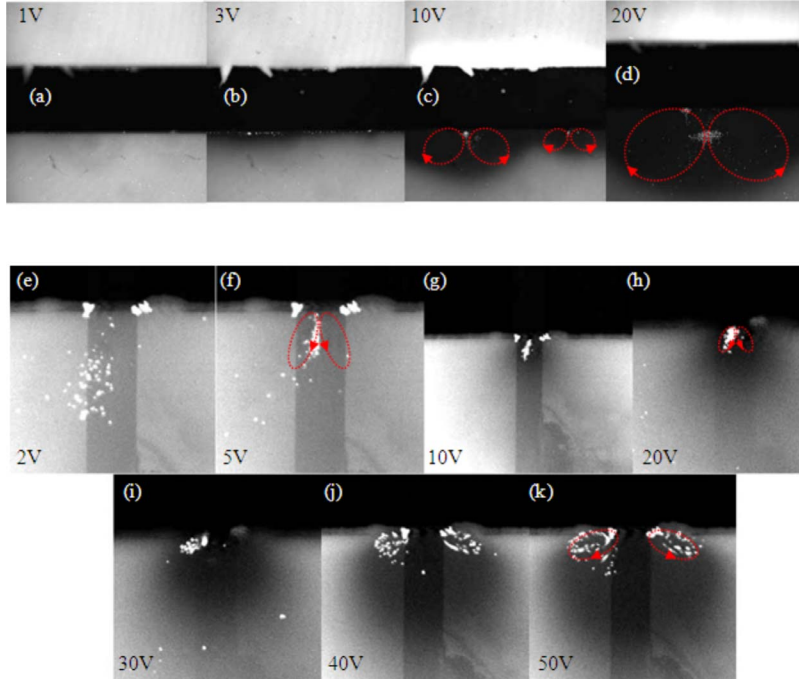


FIG. 8. (Color online) Similarly to Fig. 5—confocal image snapshots were taken of the quasisteady depletion layer occurring at the anodic entrance of the widest (a)–(d) and narrowest ($50\ \mu\text{m}$) (e)–(k) nanoslots at varying applied voltages. However, in addition to the Rhodamine dye molecules, fluorescently tagged $1.2\ \mu\text{m}$ (0.02% volumetric concentration) were added to the electrolyte solution ($10^{-5}\ \text{M}$ KCl) in order to visualize the flow dynamics, and in particular, the resulting vortex pairs (sketched schematically based on the supplementary videos [19]). In contrast to the narrow nanoslot case, wherein only a single pair of vortex can be observed, multiple vortex pairs are observed in the wide nanoslot case before they merge into a single large vortex pair (d) for large enough voltages.

loids tend to accumulate. They eventually synchronize and coalesce in a complex manner to create a single (thicker) depletion layer and a single (larger) vortex pair at large enough voltages (see the transition from Figs. 8(c) and 8(d) and the supplementary video [19]). In contrast, the depletion side of the narrow nanoslot always produces a single vortex pair [Figs. 8(e)–8(k)] at the nano-microchannel junction corners (see the schematic vortex streamlines and the supplementary video [19]). Since the colloids mirror the background flow, they follow the closed-streamline patterns of the vortex pair and tend to accumulate there. Hence, the accumulation of colloids, as seen also in the stills pictures of Fig. 8, is an indication of the existence of a vortex there. Interestingly, an elevated voltage does not only increase the size of the depletion region, and its associated vortex pair, but also tilts the vortex pair toward the horizontal plane consisting of the nanoslot entrance [compare the schematic vortex streamlines of Figs. 8(h) and 8(k)]. Furthermore, the vortex pair appears at the narrower slots before the emergence of the depletion layer [see Figs. 8(e) and 8(f) and the supplementary video [19]]. This suggests that the single vortex pair of the narrow slots originates from a mechanism different from the initial vortex array in the wider slots. The latter is most likely due to the SCL instability ([15,12,18]) but the dominant corner effects of the former suggests that corner polarization (e.g., ICEO [20,21]) at low voltages and space charge emergence concurrent with large tangential electric field component [22] (due to the field-focusing geometry) at higher voltages ($>10\ \text{V}$) are responsible for the vortex pair generation of narrow slots. This vortex pair enhances the ionic current through the nanoslot [as seen in Fig. 4(b)], as its mixing action reduces the selected CPL length scale [12].

For a sufficiently large depletion layer length relative to the nanoslot width, the three-dimensional field-focusing results in an almost spherically shaped depletion layer. More precisely, for the fabricated narrow nanoslot [Fig. 9(a)], it is

a quarter of a sphere as the bottom surface of the chip behaves as a symmetry plane. This observation allows us to produce a simple model that connects the narrow nanoslot to the nanopore. Both share the same field-focusing behavior, but with different radial geometries, and the quarter-sphere depleted region of the nanoslot is exactly one half of the half-sphere region in front of the nanopore [Fig. 9(b)].

We find the thickness of the depletion layer at one entrance to be comparable to that in the enrichment region in the other. However, due to the low ionic strength in the depletion layer, it is quite obvious that it is the depletion layer that controls the current and the thickness of both layers. The vortices and the resulting constrained depletion layer only appear beyond a critical voltage of about $10\ \text{V}$ [Figs. 8(c) and 6] and $5\ \text{V}$ [Figs. 8(e) and 6] for the wide and narrow nanoslots, respectively. Below this voltage, the CPL extends to the electrode and beyond it the vortex pair selects a smaller CPL dimension that increases monotonically with voltage, as shown in Figs. 6 and 8.

III. THEORETICAL MODEL

A nonideal permselective membrane necessitates a model for membranes of finite conductance and a theory that couples all three domains of the problem (i.e., both the CPLs at the anodic and cathodic sides of the membrane, and the nanopore). We employ Manazanares *et al.*'s simplified model [14] for a nonideally permselective nanoporous membrane, in which the surface charge is included in the averaging of the ion transport and Poisson equations across both solid and liquid phases to produce an effective homogeneous model. The membrane is assumed to contain fixed charged groups at a uniform volumetric concentration density Σ . This approach was previously used for the case of a wide nanoslot [9], but here it is extended to the axisymmetric nanopore geometry [Fig. 9(b)] with matching conditions at the entrance to cap-

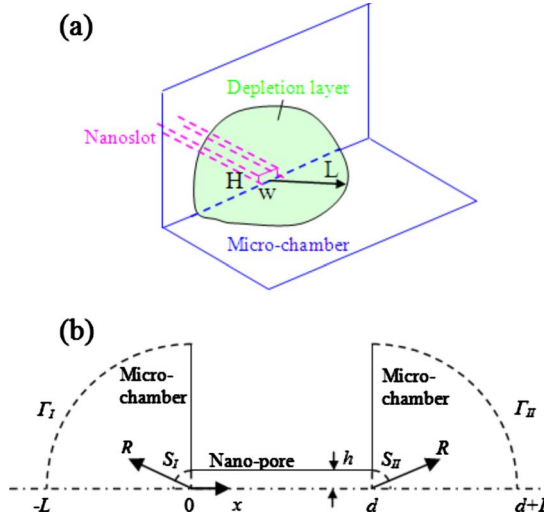


FIG. 9. (Color online) Schematic description of the three-dimensional (a) narrow nanoslot geometry and (b) axisymmetric two-sided micro-nanopore junction. When the depletion region extent L is much larger than that of the nanoslot width w , the field-focusing effect at the nanoslot resembles that of the nanopore. However, instead of the depletion region being half a sphere, it is a quarter of a sphere in the former case.

ture the field-focusing effect in the bounding reservoirs (microchambers) that arises from the three-dimensionality of the nanopore. The same field-focusing effect also occurs for true membranes consisting of widely separated nanopores but has yet to be scrutinized.

Figure 9(b) depicts schematically the two-sided axisymmetric micro-nanopore junction problem geometry *viewed in profile*. We use a spherical coordinate system (R) in the microreservoirs and a Cartesian coordinate system (x) inside the intra-nanopore. The three-dimensional problem can be further simplified into an effective one-dimensional problem, by assuming radial symmetry in the microchamber regions and treating only axial changes within the nanopore region. This assumption is valid because the nanopore radius, h , is much smaller than the dimensions of the microreservoir.

In the Ohmic region wherein the nanopore/nanoslot resistance dominates over that of the microreservoirs, it is only the former parameters (i.e., cross-section area, A , length, d , and volumetric fixed charge density Σ) that control the conductance of the entire system. The parameter Σ depends on the nanopore radius h (or nanoslot height, H) and the surface charge density. The latter, unless chemically modified, is usually predetermined by the surface chemistry of the fabri-

cation process. Hence, for the same Σ , the nanopore [Fig. 9(b)] and nanoslot [Fig. 9(a)] conductance are related to each other by the ratio of the nanopore (πh^2) to nanoslot (wH) cross-section area. As for microfabricated nanoslot $w \gg H, h$, this ratio is $\sim h/w \ll 1$.

In the non-Ohmic regions (i.e., limiting-resistance and overlimiting regions) the differential resistance is determined mainly by processes occurring outside the nanochannel/nanopore. A narrow nanoslot of width that is much smaller than the depletion layer length (i.e., $w \ll L$) can be effectively described as a point source/sink in terms of the field-focusing effect as in the case of a nanopore. Hence, for large enough depletion length, the nanoslot and nanopore non-Ohmic differential resistances are again related by the ratio of their cross-section area. It is obvious that a narrow nanoslot (i.e., $w \leq L$) cannot be modeled anymore by the two-dimensional approach which is only applicable for wide nanoslots (i.e., $w \gg L$) [9]. Instead, the three-dimensional field-focusing effect can be captured by the more simplified axisymmetric nanopore geometry as described in the following.

Both the enrichment region and the depletion region in the two entrances are assigned the CPL length L . By appropriate coordinate transformation (i.e., $x = -R$ at $-L < x < -h$, and $x = d + R$ at $d + h < x < d + L$, where L is the CPL length and d is the nanopore length) we can describe all three domains in terms of one axial coordinate x . We chose the following normalization for the axial coordinate $\tilde{x} = Lx$, ionic concentration $\tilde{c} = c_0 c$, electric potential $\tilde{\phi} = (RT/zF)\phi$, ionic flux $\tilde{j} = (Dc_0/L)j$ and electric current density $\tilde{i} = (FzDc_0/L)i$. Here, the tilda stands for dimensional parameters, c_0 is the buffer solution concentration, F denotes the Faraday number, z the ion valency, R the universal gas constant, T the absolute temperature, and D the ionic diffusion coefficient. We also define the nondimensional parameter $\delta = \lambda/L$ as the ratio between the EDL length scale, $\lambda (= \sqrt{\epsilon_0 \epsilon_f RT / 2z^2 F^2 \tilde{c}})$ and the CPL length L . Herein, ϵ_0 is the electric permittivity of vacuum and ϵ_f denotes the dielectric constant of the electrolyte solution.

As is true for most micro- and nanochannel dimensions and applied voltages, convection effects can be discarded (i.e., negligible Peclet number). A symmetric electrolyte ($z^+ = -z^- = z$) of equal diffusivities ($D^+ = D^- = D$) is assumed to simplify the analysis. Thus, ϕ and c^\pm satisfy the following (Nernst-Planck) equations for the ionic species in the three domains, with radial symmetry invoked in the microreservoirs,

$$\frac{\partial c^\pm}{\partial t} = \begin{cases} \left(\frac{\partial}{\partial x} + \frac{2}{x} \right) \left(\frac{\partial c^\pm}{\partial x} \pm c^\pm \frac{\partial \phi}{\partial x} \right) & \text{at } -1 < x < -\frac{h}{L} \\ \frac{\partial}{\partial x} \left(\frac{\partial c^\pm}{\partial x} \pm c^\pm \frac{\partial \phi}{\partial x} \right) & \text{at } -\frac{h}{L} < x < \frac{d+h}{L} \\ \left(\frac{\partial}{\partial x} + \frac{2}{x-d/L} \right) \left(\frac{\partial c^\pm}{\partial x} \pm c^\pm \frac{\partial \phi}{\partial x} \right) & \text{at } \frac{d+h}{L} < x < \frac{d+L}{L} \end{cases}, \quad (1)$$

and the corresponding Poisson's equation for the three domains are

$$\begin{cases} \frac{1}{x^2} \frac{\partial}{\partial x} \left(x^2 \frac{\partial \phi}{\partial x} \right) = -\frac{c^+ - c^-}{2\delta^2} & \text{at } -1 < x < -\frac{h}{L} \\ \frac{\partial^2 \phi}{\partial x^2} = -\frac{c^+ - c^- - \Sigma}{2\delta^2} & \text{at } -\frac{h}{L} < x < \frac{d+h}{L} \\ \frac{1}{(x-d/L)^2} \frac{\partial}{\partial x} \left[\left(x - \frac{d}{L} \right)^2 \frac{\partial \phi}{\partial x} \right] = -\frac{c^+ - c^-}{2\delta^2} & \text{at } \frac{d+h}{L} < x < \frac{d+L}{L} \end{cases}, \quad (2)$$

where Σ is the effective fixed volumetric charge (normalized by c_0) from surface charge that allows a one-dimensional formulation within the nanopore [14]. At the interface between the diffusion layer and the Ohmic bulk solution (i.e., $R=L$) ϕ and c^\pm satisfy the electrostatic conditions

$$\frac{\partial \phi}{\partial x} = -I/4\pi \quad \text{at } x = -1(\Gamma_I), \quad (3a)$$

$$\phi = 0 \quad \text{at } x = 1 + d/L(\Gamma_H), \quad (3b)$$

and the equality of the ionic concentrations to that of the buffer solution concentration c_0

$$c^\pm = 1 \quad \text{at } x = -1(\Gamma_I), \quad x = 1 + d/L(\Gamma_H). \quad (4)$$

In Eq. (3) I is the imposed electric current through Γ_I which is positive in the positive x direction. Furthermore, for future reference, the electric potential drop across the system (i.e., between Γ_I and Γ_H) is designated as V .

At the interface between the nano- and microchannels (i.e., $R=h$) we impose the matching conditions of electric field E and ionic flux j^\pm continuity to capture the field and flux focusing effects,

$$\begin{cases} (E)_R = (E)_x/2 & \text{at } x = -h/L(S_I), \quad x = d/L + h/L(S_H) \\ (j^\pm)_R = (j^\pm)_x/2 & \end{cases} \quad (5)$$

IV. FIELD-FOCUSING EFFECT

An analog of Levich's limiting-current density can be theoretically estimated for this geometry by including intraslot resistance and geometric field-focusing effects, as a first-order approximation of the limiting-resistance region in Figs. 1(a) and 4(a). This limiting current occurs when the ionic concentration at the anodic nanopore-electrolyte interface ($x=-h/L$) vanishes when the electroneutrality condition ($c^+ = c^- = c$) is employed to describe the ionic transport within the diffusion layer. Hence, the resulting ionic fluxes at the anodic side of the nanopore are

$$j^\pm = - \left(\frac{\partial c}{\partial x} \pm c \frac{\partial \phi}{\partial x} \right), \quad (6)$$

wherein j^\pm is positive in the positive x direction, from which one obtains for the spherical geometry outside the nanopore

$$\frac{\partial c}{\partial x} = -\frac{j^+ + j^-}{2} = -\frac{J^+ + J^-}{4\pi x^2}, \quad (7)$$

wherein $J^\pm = 2\pi x^2 j^\pm$ is the steady ionic flux (positive in the positive x direction) through the surface of half a sphere of $R=-x$ and the x term in the denominator on the right captures the field and flux focusing effects of the spherical geometry.

Combining Eqs. (7) and (4) yields the following nonlinear concentration profile in the DL [see Fig. 10(a)]:

$$c = 1 + \frac{J^+ + J^-}{4\pi} \left(1 + \frac{1}{x} \right) \quad \text{at } -1 < x < -h/L, \quad (8)$$

and that of the electric potential

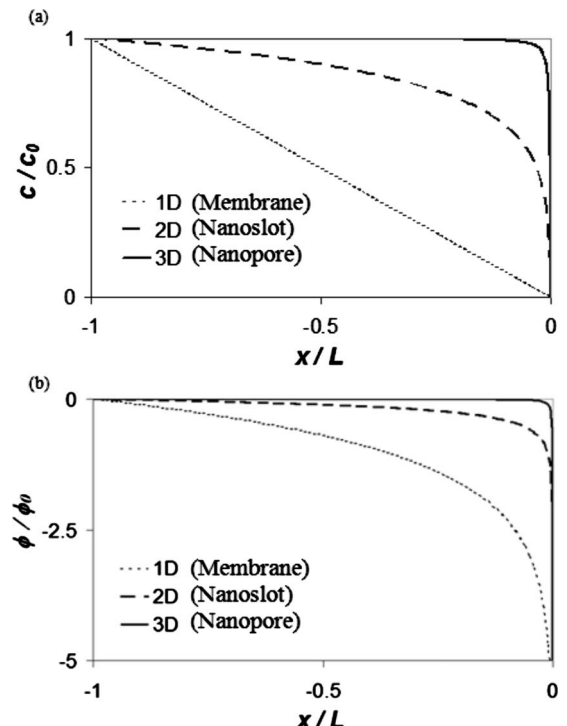


FIG. 10. Analytical results for the limiting-current conditions depicting the: (a) concentration and (b) potential profiles at the anodic side of a pseudo-one-dimensional membrane, two-dimensional nanoslot, and three-dimensional nanopore, exhibiting an increasing field-focusing effect.

$$\phi = \ln \left[1 + \frac{J^+ + J^-}{4\pi} \left(1 + \frac{1}{x} \right) \right] \left(\frac{\eta + 1}{\eta - 1} \right) \quad \text{at} \quad -1 < x < -h/L. \quad (9)$$

Imposing the limiting-current condition $c=0$ at $x=-h/L$ (S_1) on Eq. (8) yields $J^+ + J^- = 4\pi(h/L)/(1-h/L)$. The spherical geometry that focuses the field into the nanopore is responsible for a large reduction in the current corresponding to the ratio of the nanopore radius to the diffusion layer thickness, h/L , which is typically on the order of 10^{-4} . This electric current $I = J^+ - J^-$ results in the following expression for the limiting current (normalized by $FzDc_0$)

$$I_L = 4\pi \left(\frac{h/L}{1-h/L} \right) \left(\frac{\eta + 1}{\eta - 1} \right), \quad (10)$$

wherein $\eta = -J^+/J^-$ is the ratio between the counter- and co-ions fluxes (assuming that the nanopore surface is negatively charged) and is related to the permselectivity of the nanopore. For an ideal permselective nanopore (i.e., $\eta \rightarrow \infty$) we obtain $I_L|_{\eta \rightarrow \infty} = 4\pi[h/L/(1-h/L)]$. Following Manazanares *et al.* [14] [Eq. (16)] η is related to Σ through the ratio of the counter- to co-ions concentration *within* the membrane $\eta = c^+(\Sigma)/c^-(\Sigma)$ at $-h/L < x < d/L + h/L$, wherein explicit expressions for $c^\pm(\Sigma)$ are given in Eq. (17). It is obvious from Eq. (2) that within the membrane nanopore this ratio increases with Σ . Also, from Eq. (10) it is clear that the normalized limiting-current I_L monotonically increases as the permselectivity degree η decreases.

In contrast, for the pseudo-two-dimensional wide nanoslot case studied in [9], the nonlinear concentration and potential profiles in the DL are

$$c = 1 + \frac{J^+ + J^-}{\pi} \ln(-x) \quad \text{at} \quad -1 < x < -H/L, \quad (11)$$

$$\phi = \ln \left[1 + \frac{J^+ + J^-}{\pi} \ln(-x) \right] \left(\frac{\eta + 1}{\eta - 1} \right) \quad \text{at} \quad -1 < x < -H/L, \quad (12)$$

while the limiting current (normalized by $FzDc_0$) is

$$I_L = -\frac{\pi}{\ln(H/L)} \left(\frac{\eta + 1}{\eta - 1} \right). \quad (13)$$

For the pseudo-one-dimensional membrane ([9,14]) the familiar linear concentration profile and potential profile in the DL is

$$c = 1 - \frac{J^+ + J^-}{2}(x + 1) \quad \text{at} \quad -1 < x < 0, \quad (14)$$

$$\phi = \ln \left[\left(1 - \frac{J^+ + J^-}{2}(x + 1) \right) \left(\frac{\eta + 1}{\eta - 1} \right) \right] \quad \text{at} \quad -1 < x < 0, \quad (15)$$

while the limiting-current density (normalized by $FzDc_0/L$) is

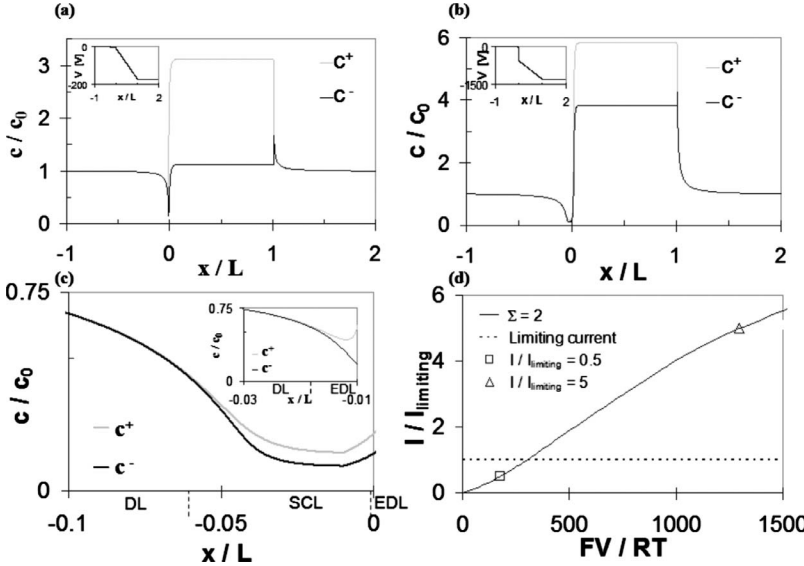
$$I_L = 2 \left(\frac{\eta + 1}{\eta - 1} \right), \quad (16)$$

with the familiar asymptotic limit of $I_L=2$ for an ideal permselective membrane ($\eta \rightarrow \infty$) (e.g., [13]). The extra algebraic term in the nanopore case in Eq. (10) and the logarithm geometric term in the nanoslot case in Eq. (13) are due to the field-focusing effects of the two different geometries. It is clear that both serve to lower the limiting-current density but the difference is more pronounced for the nanopore.

However, the limiting-current density in Eq. (10) only estimates the current density at the limiting-resistance region and not its differential resistance. The dominance of intraslot resistance occurs because of field focusing into the nanopore—all the current must go through the nanopore and the converging field produces a high current density from the bulk in Eq. (10) that increases with the large ratio of the CPL thickness to the nanochannel height. To sustain this high Ohmic current from the bulk, a polarized layer develops as the bulk concentration at the interface approaches zero to introduce a larger field for flux into the pore [8]. With the appearance of the polarized layer, the electroneutral assumption of the limiting-current theory breaks down and a finite differential resistance develops at the anodic CPL.

The development of the polarized region can be captured numerically using the above pseudo-one-dimensional formulation (1), (2), (3a), (3b), (4), and (5). The distinct DC ion distributions and I - V characteristics in the Ohmic and overlimiting-current regimes are demonstrated for the axisymmetric geometry of a nanopore in Fig. 11. All computations are done with one specific CPL thickness L . Note that the depletion side on the left, where the bulk concentration c approaches zero, controls the I - V characteristics and contains significant space charge in its EPL. The enrichment side on the right with an ionic concentration higher than the bulk is always electroneutral (outside the thin equilibrium EDL) without a polarized layer. It is this polarized layer, amplified by the field-focusing effect, on the depletion side that invalidates the classical limiting-current theory involving only electroneutral bulk transport.

The varying field-focusing intensities in terms of the ionic concentration and potential profiles on the anodic side of the membrane/nanoslot/nanopore are depicted in Figs. 10(a) and 10(b), respectively. It is quite clear that when shifting from a pseudo-one-dimensional to a three-dimensional field-focusing geometry, the gradients near the nanochannel interface becomes more severe, resulting in most of the ionic concentration and potential drop to occur there. Hence, for the pseudohomogenous membrane case, it is the vortex instability that is responsible for selecting a much smaller CPL length scale (which otherwise goes all the way to the electrode). However, in the nanopore case, it is the geometrical three-dimensional field-focusing effect that effectively dictates a significantly smaller CPL, which is weakly dependent on the nanoslot-electrode distance. For nanopores, the role of the corner vortices in sustaining this small CPL length scale is probably not as significant as that of the vortex instability array in the former case.



V. OHMIC REGION OF THE I-V CURVE

From the insets of Figs. 11(a) and 11(b), it is clear that the resistance is negligible in the cathodic enrichment side and the intraslot and CPL layer resistance on the anodic depletion side control the ion current flux. The anodic CPL resistance is further broken down into two parts: SCL and DL. As is evident in Fig. 11(a) and inset of Fig. 11(c), the SCL layer does not exist in the Ohmic region of the I - V curve. With field focusing, nanoslot/nanopore resistance dominates over DL resistance in the Ohmic region as seen in the inset of Fig. 11(a). As the conductance of the nanoslot in the low concentration limit is specified by the total surface charge, the resistance in this region has a very different dependence on the ionic strength for a slot whose height is much larger than the Debye layer [Fig. 1(b)].

We analyze the Ohmic region of the nanoslot data in Fig. 1(a) to obtain the surface charge density in the form of Σ in the model of Eq. (2). The DC conductance was determined by fitting the slope of the ionic current as a function of the applied voltage [Fig. 1(a)]. At high c_0 , where $\kappa H \gg 1$ ($\kappa = \lambda^{-1}$), the conductance $\tilde{I}/\tilde{V} = 2zF\mu c_0 wH/d$ is linear with c_0 , as is consistent with bulk electrolyte conductance. At low c_0 , where $\kappa H \ll 1$ and the surface charge density is $2|\sigma| \gg zFc_0H$, the conductance is independent of H and c_0 , behaving as $\tilde{I}/\tilde{V} \approx 2|\sigma|\mu w/d$ (wherein $\mu = zF\nu = zFD/(RT)$ is the ion mobility, w is the nanoslot width, d is the nanochannel length and the factor 2 stands for both the top and bottom walls of the nanoslot while the side walls are neglected). The constant conductance reflects the fact that the nanoslot ions are mostly counterions and, due to electroneutrality, their number is equal to the total surface charge independent of bulk ionic strength or slot height. As is consistent with our model, conductance enhancement due to electro-osmosis has been neglected. For the nanoslot parameters [Fig. 9(a)] $H \sim 200$ nm, $d = 500$ μm , $w = 2$ mm, and KCl solution parameters $z = 1$, $\mu = 7.6 \times 10^{-8}$ $\text{m}^2/\text{V s}$ [25], a fitted value of $|\sigma| = 7$ mC/m² for the surface charge density (inside the measured surface charge density range of 2–100 mC/m²

FIG. 11. Numerical computation results for the concentration-polarization profiles across an axisymmetric nanopore ($0 \leq x \leq 1$) for currents below (a) and beyond (b) the limiting-current I_L . The insets of parts (a) and (b) of the figure describe the potential drop across the system. Part (c) of the figure depicts the ion concentration profiles on the anodic side of the nanopore for the overlimiting conditions of (b), exhibiting an SCL, in contrast to the profile of (a) in the inset. Also depicted are the electroneutral DL and the EDL. The I - V curve for the membrane, exhibiting an inflection point at I_L , is shown in (d) with the conditions for (a) and (b) indicated. The normalized values of $\Sigma = 2$, $d = 1$, $h/L = 10^{-2}$, and $\delta = 10^{-3}$ have been used.

reported in [26] for similar substrates) was obtained from the low c_0 data of Fig. 1.

Following Manazanares *et al.* [14], we substitute the surface charge density, σ , by a fixed volume charge density $zF\tilde{\Sigma} = -2\sigma/H$ for the nanoslot case of about 74 KC/m³. Based on the well-known Donnan equilibrium relations [14], the ionic concentrations *within* the nanoslot can be expressed as

$$\tilde{c}^\pm = \pm \tilde{\Sigma}/2 + \sqrt{(\tilde{\Sigma}/2)^2 + c_0^2} \quad \text{at } 0 \leq \tilde{x} \leq d. \quad (17)$$

This produces a universal ionic conductance [27] for the intraslot dominating Ohmic region,

$$\tilde{I}/\tilde{V} = (F^2 \sum_i z_i^2 \nu_i \tilde{c}_i) wH/d = 2F\mu \sqrt{(\tilde{\Sigma}/2)^2 + c_0^2} wH/d, \quad (18)$$

which reduces to $\tilde{I}/\tilde{V} = 2zF\mu c_0 wH/d$ in the limit of high concentrations, $c_0 \gg \tilde{\Sigma}$, and to $\tilde{I}/\tilde{V} \approx zF\mu \tilde{c}^+ wH/d = -2\sigma\mu w/d$ in the limit of low concentrations, $c_0 \ll \tilde{\Sigma}$. As seen in Fig. 1(b), a good agreement is obtained between the model (18) (thin black continuous line) and the experimentally measured Ohmic data. Also depicted in Fig. 1(b) is the expected bulk conductance (thin black dashed line) as obtained from model (18) while neglecting the effect of the nanochannel surface charge, i.e., $\tilde{\Sigma} = 0$. A clear deviation from this bulk conductance is clearly seen to occur at concentrations of about 1 mM, indicating that ion permselective effects become dominant at ionic strengths below this value.

Applying the model (1), (2), (3a), (3b), (4), and (5) of an axisymmetric nanopore to the narrow nanoslot requires to somewhat relate between the two different geometries, that mainly differ by the large ratio of cross-section areas, as the length, d , may be of the same order. Taking the nanopore model to have the same parameters d , σ , and $\tilde{\Sigma}$ as those of the narrow nanoslot chip, dictates the nanopore radius h to be according to the relation $zF\tilde{\Sigma} = -2\sigma/h$. Hence, according to Eq. (18), the nanoslot and nanopore Ohmic conductance are related by a factor of cross-section area ratio ($wH/\pi h^2$).

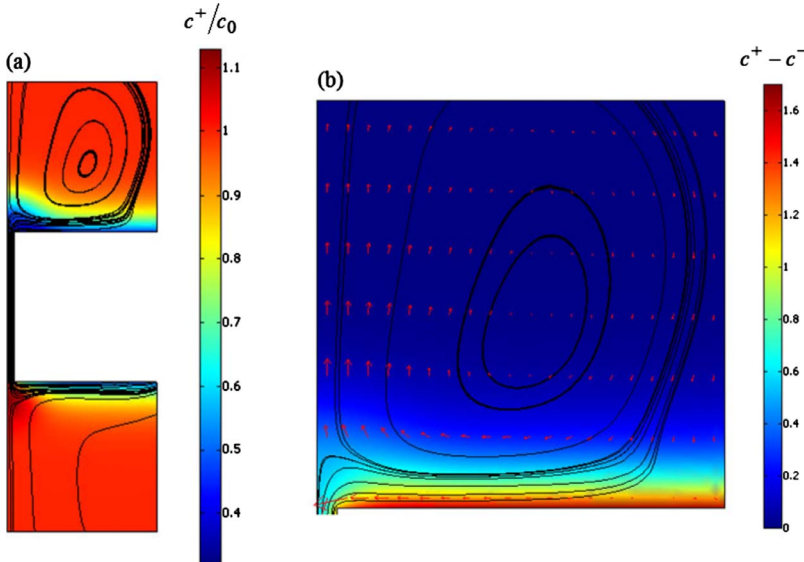


FIG. 12. (Color online) (a) Finite-element numerical simulation of the electrokinetic flow for an axisymmetric nanopore system bounded by two microreservoirs (continuous lines—streamlines; surface plot—normalized co-ions concentration). Note the enrichment-depletion of the co-ions at the cathodic/anodic entrances, respectively. (b) Close up of the anodic side showing that the direction of the vortex rotation is opposite from that predicted for Rubinstein's instability vortex pair [15]. (continuous lines—streamlines; vectors—velocity field; surface plot—normalized net ionic charge density).

VI. NON-OHMIC REGIONS OF THE I-V CURVE

In contrast to the Ohmic region, wherein the field-focusing effect is of no importance at all since it is only the nanochannel part that controls the current, the non-Ohmic region current strongly depends on the degree of field focusing at the channel entrance. This understanding combined with the mechanism of selecting the diffusion layer (CPL) length scale was recently used by us [9] to provide the first comprehensive quantitative explanation of the nonlinear I - V curve consisting of the three distinct regions (Ohmic, limiting resistance and overlimiting) for the wide nanoslot case. The same approach, but this time using the three-dimensional field-focusing model (1), (2), (3a), (3b), (4), and (5) in Sec. III, can be applied for the narrow nanoslot data of Fig. 4.

In contrast to the wide nanoslot case with a very wide voltage window for the limiting-resistance region (Fig. 4) bounded between the linear Ohmic and overlimiting regions, the narrow nanoslot does not exhibit a discernable limiting-resistance region. It is quite obvious that with decrease of the nanoslot width, the system nonuniformity increases, as boundary effects associated with the nanoslot sidewalls becomes more pronounced. One obvious consequence of this nonuniformity is the emergence of corner vortices [Figs. 8(e)–8(k)] that are quite distinct from Rubinstein's vortex array instability away from the corners [15]. This suggests that the vanishing of the limiting-resistance region is intimately connected to increase of the system nonuniformity.

For channels without permselectivity or an extended polarized layer, corner vortices are attributed to induced-charge polarization of the corners [20,21] when charge build-up at the corners produces a large converging flow. In the current case of the nanopores, a localized space charge region exists at the pore entrance and the focusing field toward the pore (i.e., non-negligible tangential field component) can impart a converging (toward the nanopore entrance) Maxwell body force on the liquid at the space charge region [22]. Since the similitude between the electric and velocity fields [28] breaks, once the extended polarized layer kicks in, and

hence, also the fluid irrotational behavior, flux continuity arguments dictates that the excess flux at the microchamber side (over that through the nanopore) produce a vortex similar to the one seen in [20,21].

The finite element based numerical simulation results shown in Fig. 12 indeed predict such a vortex (actually, a torus with an axis corresponding to the axial coordinate) to appear at the depletion layer side of the axisymmetric nanopore wherein an extended polarized layer can be sustained. In the case of a planar nanochannel, it is a vortex pair that emerges from the corners. The full set of nonlinear coupled equations: Poisson's, continuity of ions (Nernst-Planck) and Stokes equations,

$$\nabla^2 \tilde{\phi} = -\frac{zF(\tilde{c}^+ - \tilde{c}^-)}{\varepsilon_0 \varepsilon_f}, \quad (19a)$$

$$\nabla \cdot \left(-D \nabla \tilde{c}^\pm \mp \frac{DzF}{RT} \tilde{c}^\pm \nabla \tilde{\phi} \right) = 0, \quad (19b)$$

$$\eta' \nabla^2 \tilde{\mathbf{u}} - \nabla \tilde{p} - zF(\tilde{c}^+ - \tilde{c}^-) \nabla \tilde{\phi} = 0, \quad \nabla \cdot \tilde{\mathbf{u}} = 0, \quad (19c)$$

assuming a small Peclet number (hence, decoupling between the electrostatic and hydrodynamic problems), was solved numerically for the axisymmetric geometry depicted in Fig. 12(a) consisting of a nanopore connecting two opposite microreservoirs. Herein, \mathbf{u} is the velocity vector, η' is the dynamic fluid viscosity and p is the hydrodynamic pressure. Far field conditions included an applied potential difference, bulk ionic concentration and zero pressure difference. At the walls, an equilibrium surface charge density was taken, together with the ion impermeability and the no-slip boundary conditions.

The resulting toroidal vortex has a direction of rotation that is in agreement to that observed experimentally [compare Fig. 12 with Fig. 8(k)]. We note that the focusing tangential field in the direction of the flow can be screened by neighboring pores and hence the onset of these ejecting vor-

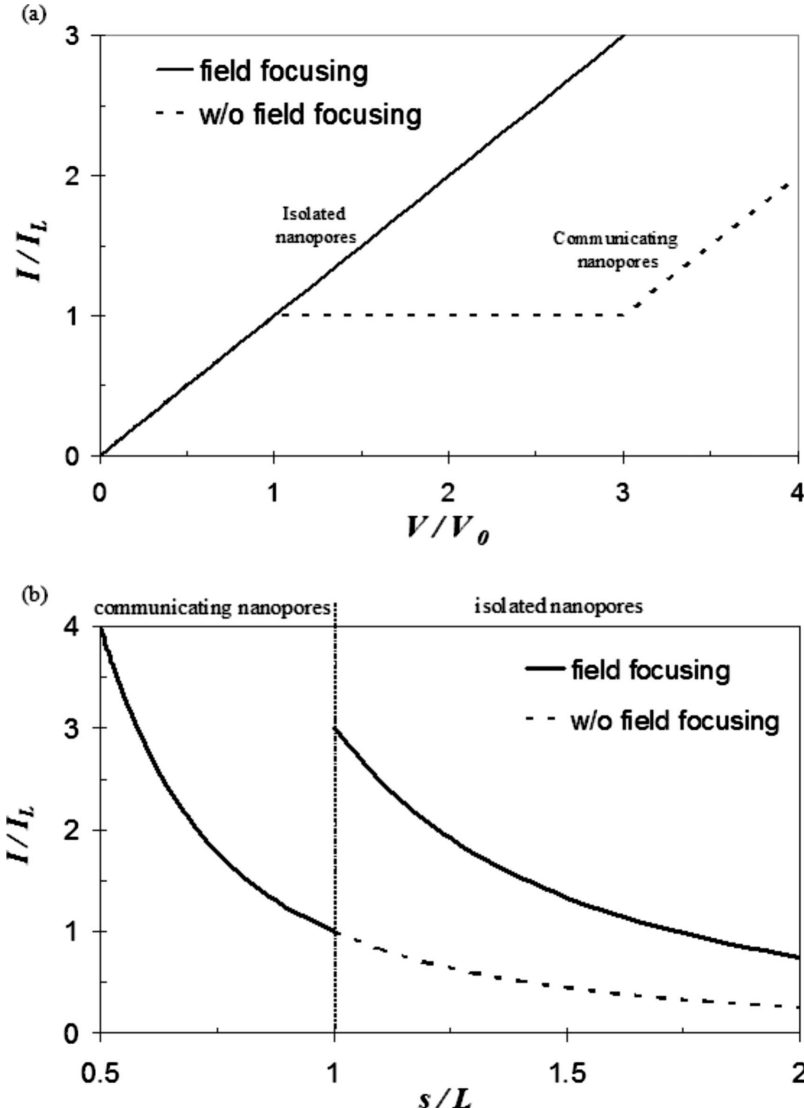


FIG. 13. (a) Normalized [by I_L of Eq. (16)] current versus the normalized [by V_0 of Eq. (20)] applied voltage for identical number of nanopores in either isolated (with field focusing) or communicating (i.e., nanoporous membrane, w/o field focusing) mode. The overlimiting resistance is approximated as equal to that of the Ohmic region. An arbitrary voltage window of $2V_0$ is taken for the limiting-resistance region of a nanoporous membrane. This conceptual figure should be compared to the experimental data of Fig. 4(b); (b) Normalized current versus the normalized (by the selected CPL length L) pore-pore separation distance s for the case of isolated and communicating nanopores, as obtained from part (a) of the figure, for the particular case of $V/V_0=3$. A clear local maximum of the current is seen around the transition value of $s/L=1$.

tices should be a function of the pore separation. In contrast, the wide slot has an extended space charge region in the lateral direction and the same mechanism would have produced a single vortex cylinder with a vorticity direction orthogonal to the observed ones. The vortex array for the wide slot due to Rubinstein's instability, on the other hand, has a vorticity vector that is antiparallel to the observed one and is not due to boundary effect. This suggests that the ejecting vortex torus is unique to the narrow pore and, unlike an instability, it exists for all voltages beyond the threshold voltage of the Ohmic to limiting-resistance transition associated with the occurrence of SCL. This is consistent with the early [Fig. 8(f)] detectable occurrence of the vortex pair for narrow slots and its absence of a limiting-resistance region, which produces a direct transition from Ohmic to overlimiting regions.

This observation of vanishing limiting-resistance region is incorporated in the theoretical model of the nanopore (narrow nanoslot) wherein the critical voltage for the overlimiting region is shifted to coincide that of the threshold voltage due to the development of the SCL, as the controlling resistance switches from the intraslot region (Ohmic) to the po-

larized layer region (limiting resistance). This threshold voltage is estimated from the dimensional versions of the limiting-current Eq. (10) and the nanopore conductance (18) as

$$V_0 = 2zDc_0L \left(\frac{h/L}{1-h/L} \right) \left(\frac{\eta+1}{\eta-1} \right) (\mu \sqrt{(\tilde{\Sigma}/2)^2 + c_0^2 h^2/d})^{-1}. \quad (20)$$

As most of the voltage drop shifts from the intraslot to the external polarized layer, when an Ohmic to overlimiting-current transition occurs, this suggests that the nanoslot entrance geometrical properties become much more important than its length d . Hence, the appropriate translation between the narrow nanoslot and the nanopore overlimiting conductance is the ratio of the cross-section areas, in contrast to the Ohmic case in which it is the ratio of the cross-section area divided by the channel length [A/d , see Eq. (18)].

VII. CONCLUDING REMARKS

Thus, using different geometrical models we have shown experimentally and theoretically (Fig. 10) that, due to the

enhanced field-focusing effect of a pointlike nanopore, the concentration-polarization (and potential) gradients become more severe with decreasing nanoslot entrance width. One of the consequences of the isolation is a single localized depletion region in the narrow nanoslot case, instead of an array of them in the wide nanoslot case due to an instability. This isolated space charge region at the pore entrance produces an ejecting vortex pair for isolated narrow nanochannels (Fig. 8) or a vortex toroid for isolated nanopores (Fig. 12). An important consequence is the vanishing of the limiting-resistance window in the narrow nanoslot (Fig. 4) in contrast to a very clear region in the wide nanoslot case, thus producing very high current density for all voltages that are not limited by Levich's diffusion-limited current [2]. By using varying nanoslot widths, we were actually able to capture the gradual vanishing of the limiting-resistance window with decreasing width (Fig. 4).

An intriguing question is when the nanopores of a nanoporous membrane are effectively isolated and exhibit point-like field-focusing effect studied here. From our analysis, the depletion layer at the limiting-current of an isolated nanopore extends to $\sim 0.1L$ (contains 99% of the concentration drop. See Figs. 10, 3D) and hence a good estimate would be that this is the minimum pore separation to eliminate pore-pore interaction [29,30]. Since the current scales linearly

with the total pores area, for a fixed pore radius, the current is inverse proportional to the quadrate of the pore-pore separation length. Thus, taking the 1D membrane limiting current as a measure of the current for pore separations smaller than the depletion layer length, and the Ohmic-like behavior of isolated nanopore as a measure of the overlimiting current (approximating the overlimiting differential resistance as that in the true Ohmic region (18)—see Fig. 4) for pore separations larger than the depletion layer [see Fig. 13(a)], we obtain Fig. 13(b). As seen, a maximum of the current occurs at an optimal pore separation (s) when it is roughly the depletion layer length (L). Although this is a sharp maximum, it is a local one as the current is higher for s/L less than 0.6. However, while small pore separations would obviously produce a larger current due to area considerations, they may correspond to mechanically unstable membranes that are difficult to fabricate.

ACKNOWLEDGMENTS

G.Y. was supported by the Taub Foundations. H.C.C. acknowledges support from NSF-IDBR under Grant No. 0852741. We are grateful to Prof. Y. Zhu and Prof. A. Seabaugh of Notre Dame for the use of their equipment and for their advice.

-
- [1] F. Maletzki, H.-W. Rosler, and E. Staude, *J. Membr. Sci.* **71**, 105 (1992).
- [2] V. G. Levich, *Physicochemical Hydrodynamics* (Prentice-Hall, New York, 1962).
- [3] D. Stein, M. Kruithof, and C. Dekker, *Phys. Rev. Lett.* **93**, 035901 (2004).
- [4] Q. Pu, J. Yun, H. Temkin, and S. Liu, *Nano Lett.* **4**, 1099 (2004).
- [5] A. Plesis, R. B. Schoch, and P. Renaud, *Nano Lett.* **5**, 1147 (2005).
- [6] R. Karnik, C. Duan, K. Castelino, H. Daiguji, and A. Majumdar, *Nano Lett.* **7**, 547 (2007).
- [7] S. J. Kim, Y. C. Wang, J. H. Lee, H. Jang, and J. Han, *Phys. Rev. Lett.* **99**, 044501 (2007).
- [8] I. Rubinstein and L. Shtilman, *J. Chem. Soc., Faraday Trans. 2* **75**, 231 (1979).
- [9] G. Yossifon, P. Mushenheim, Y. C. Chang, and H.-C. Chang, *Phys. Rev. E* **79**, 046305 (2009).
- [10] H. Bayley and P. S. Cremer, *Nature (London)* **413**, 226 (2001).
- [11] J. Li, D. Stein, C. McMullan, D. Branton, M. J. Aziz, and J. A. Golovchenko, *Nature (London)* **412**, 166 (2001).
- [12] G. Yossifon and H.-C. Chang, *Phys. Rev. Lett.* **101**, 254501 (2008).
- [13] Y. Ben and H.-C. Chang, *J. Fluid Mech.* **461**, 229 (2002).
- [14] J. A. Manzanares, W. D. Murphy, S. Mafe, and H. Reiss, *J. Phys. Chem.* **97**, 8524 (1993).
- [15] I. Rubinstein and B. Zaltzman, *Phys. Rev. E* **62**, 2238 (2000).
- [16] B. Zaltzman and I. Rubinstein, *J. Fluid Mech.* **579**, 173 (2007).
- [17] I. Rubinstein, B. Zaltzman, J. Pretz, and C. Linder, *Russ. J. Electrochem.* **38**, 853 (2002).
- [18] S. M. Rubinstein, G. Manukyan, A. Staicu, I. Rubinstein, B. Zaltzman, R. G. H. Lammertink, F. Mugele, and M. Wessling, *Phys. Rev. Lett.* **101**, 236101 (2008).
- [19] See supplementary material at <http://link.aps.org/supplemental/10.1103/PhysRevE.81.046301> for supplementary videos.
- [20] Y. Eckstein, G. Yossifon, A. Seifert, and T. Miloh, *J. Colloid Interface Sci.* **338**, 243 (2009).
- [21] S. K. Thamida and H.-C. Chang, *Phys. Fluids* **14**, 4315 (2002); G. Yossifon, I. Frankel, and T. Miloh, *ibid.* **18**, 117108 (2006).
- [22] S. S. Dukhin, *Adv. Colloid Interface Sci.* **35**, 173 (1991).
- [23] J. Balster, M. H. Yildirim, D. F. Stamatialis, R. Ibanez, R. G. H. Lammertink, V. Jordan, and M. Wessling, *J. Phys. Chem. B* **111**, 2152 (2007).
- [24] V. G. Kutchoukov, F. Laugere, W. van der Vlist, L. Pakula, Y. Garini, and A. Bossche, *Sens. Actuators, A* **114**, 521 (2004).
- [25] *CRC Handbook of Chemistry and Physics*, 63rd ed., edited by R. C. Weast (CRC Press, Boca Raton, 1982).
- [26] R. Karnik, R. Fan, M. Yue, D. Li, P. Yang, and A. Majumdar, *Nano Lett.* **5**, 943 (2005).
- [27] R. F. Probstein, *Physicochemical Hydrodynamics—An Introduction* (Butterworths, Boston, 1989).
- [28] E. Cummings, S. Griffiths, R. Nilson, and P. Paul, *Anal. Chem.* **72**, 2526 (2000).
- [29] G. Yossifon, Y. C. Chang, and H.-C. Chang, *Phys. Rev. Lett.* **103**, 154502 (2009).
- [30] H.-C. Chang and G. Yossifon, *Biomicrofluidics* **3**, 012001 (2009).